

Article

Flower-like Co_3O_4 Catalysts for Efficient Catalytic Oxidation of Multi-Pollutants from Diesel Exhaust

Zihao Li ¹, Xianhuai Chen ¹, Jinghuan Chen ² , Huazhen Chang ³, Lei Ma ^{1,*}  and Naiqiang Yan ¹

¹ School of Environmental Science and Engineering, Shanghai Jiao Tong University, Shanghai 200240, China; lizihao6@sjtu.edu.cn (Z.L.); chenxianhuai@sjtu.edu.cn (X.C.); nqyan@sjtu.edu.cn (N.Y.)

² Key Laboratory of Microbial Technology for Industrial Pollution Control, School of Environment, Zhejiang University of Technology, Hangzhou 310014, China; chenjh20@163.com

³ School of Environment and Natural Resources, Renmin University of China, Beijing 100872, China; chz@ruc.edu.cn

* Correspondence: leima8@sjtu.edu.cn

Abstract: Nowadays, the oxidation activity at the low-temperature regime for Co_3O_4 catalysts needs to be improved to meet the stringent regulation of multi-pollutant diesel exhaust. Herein, nanoflower-like Co_3O_4 diesel oxide catalysts (DOCs) were fabricated with the addition of a low-content Pt to trigger better catalytic activities for oxidizing multi-pollutants (CO , C_3H_6 , and NO) emissions by taking advantage of the strong-metal supporting interaction. Compared to the conventional DOCs based on $\text{Pt}/\text{Al}_2\text{O}_3$, the as-synthesized $\text{Pt}/\text{Co}_3\text{O}_4$ catalysts not only exhibited better multi-pollutants oxidation activities at the low temperature but also obtained better resistance toward NO inhibition. Moreover, $\text{Pt}/\text{Co}_3\text{O}_4$ catalysts showed exceptional hydrothermal durability throughout long-term tests in the presence of water vapor. According to the XPS and H_2 -TPR results, Pt promoted low-temperature catalytic activity by increasing the active surface oxygen species and reducibility due to the robust synergistic interaction between metallic Pt and supporting Co_3O_4 . Meanwhile, TGA curves confirmed the Pt atoms that facilitated the desorption of surface-active oxygen and hydroxyl radicals in a low-temperature regime. Furthermore, instead of probing the intermediates during CO and C_3H_6 oxidation for $\text{Pt}/\text{Co}_3\text{O}_4$ catalysts, which included carbonates, formate, and acetate species, in situ DRIFTS experiments also revealed C_3H_6 oxidation mainly took place over metallic Pt sites.

Keywords: diesel oxide catalysts; catalytic oxidation; strong metal–support interaction; cobalt oxides; platinum



Citation: Li, Z.; Chen, X.; Chen, J.; Chang, H.; Ma, L.; Yan, N.

Flower-like Co_3O_4 Catalysts for Efficient Catalytic Oxidation of Multi-Pollutants from Diesel Exhaust.

Catalysts **2022**, *12*, 527. <https://doi.org/10.3390/catal12050527>

Academic Editors: Jin Chen and Xuejiao Liu

Received: 18 April 2022

Accepted: 5 May 2022

Published: 7 May 2022

Publisher's Note: MDPI stays neutral with regard to jurisdictional claims in published maps and institutional affiliations.



Copyright: © 2022 by the authors. Licensee MDPI, Basel, Switzerland. This article is an open access article distributed under the terms and conditions of the Creative Commons Attribution (CC BY) license (<https://creativecommons.org/licenses/by/4.0/>).

1. Introduction

Compared to gasoline engines, diesel engines provide higher fuel efficiency and better durability, along with much lower production of carbon dioxide (CO_2) [1], which enlarges the automobile market for diesel vehicles. However, the multi-pollutants of carbon monoxide (CO), hydrocarbons (HC), nitrogen oxides (NO_x), and diesel particulate matter (PM) emitted from the diesel engines cause severe environmental problems [2]. Diesel oxide catalysts (DOCs) are applied as the upstream element in the automobile after-treatment systems to purify the multi-pollutant emissions. As the first module in the vehicle after-treatment systems, DOCs not only convert CO and HC into CO_2 but also play a critical role in oxidizing nitrogen monoxide (NO) to nitrogen dioxide (NO_2) [3]. Due to its robust oxidizing ability, NO_2 generated from DOCs facilitates the passive regeneration of the diesel particulate filter (DPF) and promotes the selective catalytic reduction of NO_x with ammonia (NH_3 -SCR) by triggering the “fast” SCR pathway in the downstream system [4–6]. As a result, DOCs are the crucial part governing the holistic catalytic performances of the vehicle after-treatment systems. Typically, commercial DOCs apply platinum group metals (PGMs), such as Pt and Pd, as the dominant components due to their promising catalytic oxidation activities of CO and HC . However, the strong adsorption of CO and HC over

the PGMs usually poisons the active sites of DOCs, which prohibits the activation of O₂ and leads to poor catalytic activity at the cold-start stage [7]. Thus, better low-temperature catalytic oxidation performances are required for DOCs to accomplish 90% conversion at 150 °C of vehicle multi-pollutants emissions set by U.S. DRIVE [8].

In past decades, spinel-structured cobalt oxide (Co₃O₄) demonstrated excellent catalytic oxidation activities for various pollutants such as methane and volatile organic compounds [9]. Specifically, Co₃O₄ nanorods exposing adequate active sites of Co³⁺ accomplished the complete conversion of CO at −77 °C [10]. Therefore, we have developed Co₃O₄ nanorods as a potential non-PGM catalyst for diesel exhaust treatment. According to our previous studies, Co₃O₄ nanorods fabricated via the SBA-15 template exhibited excellent catalytic performances and hydrothermal stability toward NO and propane oxidation as a rival to traditional platinum DOCs [11,12]. Meanwhile, the as-synthesized Co₃O₄ nanorods also performed great catalytic activities for multi-pollutants diesel emissions [13]. However, the low-temperature catalytic activities of C₃H₆ and NO oxidation could still be improved over Co₃O₄ catalysts.

Triggering the strong metal–support interaction (SMSI) between noble metal and reducible metal oxide support is a reliable method to elevate low-temperature reactivity [14]. Kaper et al. claimed that the room-temperature CO oxidation could be achieved by the strong interaction between Pt and CeO₂ [15]. Moreover, Christopher et al. indicated that the isolated Pt supported by TiO₂ obtained better reactivity than nanoparticle Pt because of the larger interfacial area between isolated Pt atoms and supporting TiO₂, which resulted in the strong synergistic interaction [16]. Moreover, the oxygen-induced transformation at the interface of Pt encapsulated by Fe₃O₄ contributed to the better catalytic activity toward CO oxidation [17]. Other than the SMSI effect, the catalytic activities might be affected by the morphology of Co₃O₄ (nanorods, nanoparticles, nanosheets, and nanocages) [11,18,19], which indicated that the specific structures might be a feasible factor governing the catalytic activity. Recently, Chen et al. claimed that flower-structured Co₃O₄ exposing both (110) and (112) plans possessed better catalytic activity of toluene oxidation than the Co₃O₄ nanorods [20].

Herein, a nanoflower-like Co₃O₄ (coded as Co₃O₄-F) was prepared via the hydrothermal method to oxidize simulated diesel exhaust. Approximately 0.8 wt.% Pt was loaded to further improve the reactivity of C₃H₆ and NO oxidation. Initially, the catalytic performances were carried out for various catalysts of Co₃O₄-F, Pt/Co₃O₄-F, and other conventional DOCs, to compare the catalytic activities toward multi-pollutants diesel exhaust. Meanwhile, the feasibility of Pt/Co₃O₄-F as DOCs was approved during the hydrothermal durability tests under simulated diesel emissions. Moreover, the morphological properties were investigated via SEM, XPS, and N₂ adsorption–desorption isotherms. The results of XPS, H₂-TPR, and N₂-TGA were also presented in the literature to illustrate the SMSI effect between Pt and supporting Co₃O₄-F. Lastly, in situ DRIFTS experiments not only probed the specific surface intermediates during the reactions but also elucidated the function of Pt atoms in promoting the catalytic oxidation activity.

2. Results and Discussion

2.1. Catalytic Activities and Stability

The catalytic oxidation activities of CO, C₃H₆, and NO were measured over various catalysts, and the results were summarized in Figure 1. For both CO and C₃H₆ oxidation, Co₃O₄-F and Pt/Co₃O₄-F exhibited better catalytic activities than commercial Pt/Al₂O₃ catalysts. Although Pt/Al₂O₃ catalysts reached optimal NO conversions at a lower temperature, the maximum conversions of NO oxidation still decreased in the sequence of Pt/Co₃O₄-F (79.4%) > Co₃O₄-F (78.9%) > Pt/Al₂O₃ (71.6%). Since water vapor was a common component in diesel exhaust and could deactivate catalysts by blocking the active sites [21,22], high hydrothermal stability was requested for DOCs. Consequently, a long-term durability test was carried out under a simulated diesel exhaust mixture with 5% H₂O at 260 °C to investigate the hydrothermal durability of the Pt/Co₃O₄-F catalysts. As shown

in Figure 1d, the Pt/Co₃O₄-F catalysts maintained a nearly 100% CO conversion through 43-hour on-stream experiments. Meanwhile, no significant activity loss was observed in C₃H₆ oxidation, in which the conversion slightly dropped from 99.3% to 93.1%. According to the light-off results from Figure 1c, the Pt/Co₃O₄-F catalyst was supposed to achieve an approximately 74% NO conversion under a dry simulated exhaust atmosphere at 260 °C. Yet, the conversion of NO decreased to 8% on the stream, which could be due to the rapid reaction between formed NO₂ and H₂O to generate HNO₃ [23]. Fortunately, NO conversion in the presence of water vapor was relatively stable throughout the long-term hydrothermal durability tests. Overall, the catalytic performance toward multi-pollutant diesel emissions on Pt/Co₃O₄-F was sufficiently stable under the simulated exhaust condition. To further compare catalytic performance, T₅₀ and T₉₀, representing the temperatures of 50% and 90% conversion for specific pollutants, respectively, were applied. As listed in Table S1, the catalytic activities of as-synthesized Pt/Co₃O₄-F catalysts outperformed the previously reported Pt/Al₂O₃ catalysts and commercial Pt-Pd/Al₂O₃ DOCs toward multi-pollutants exhaust, which proved that the Pt/Co₃O₄-F catalyst could be a feasible choice for DOCs.

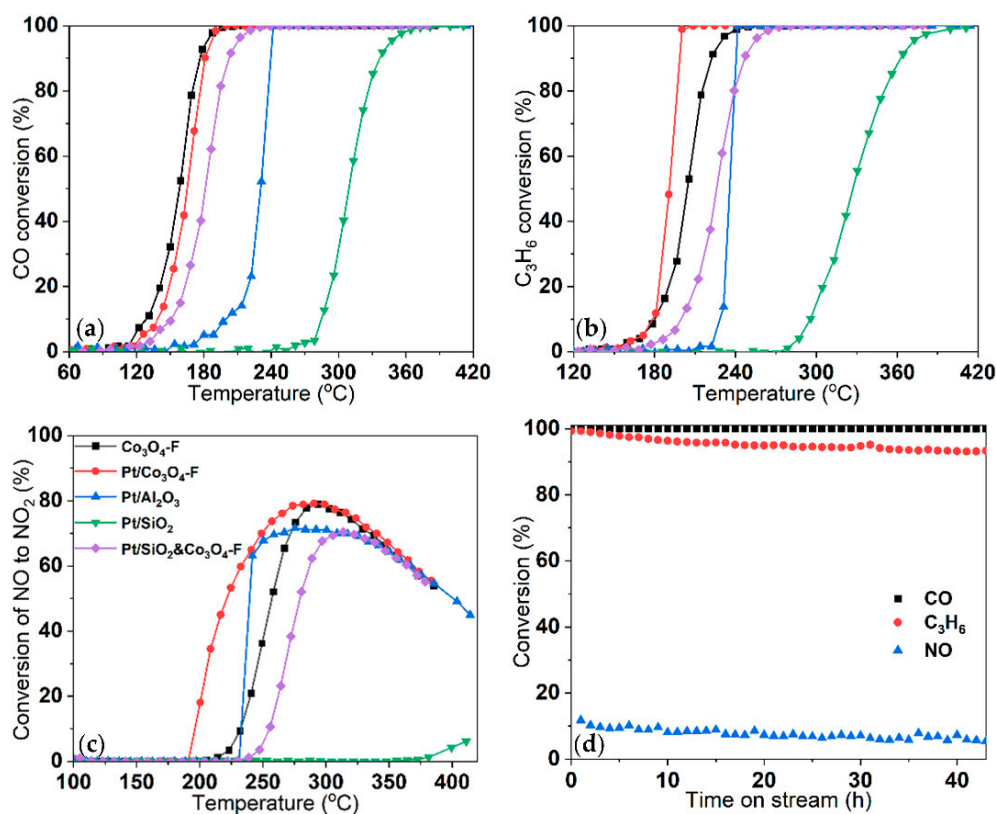


Figure 1. The light-off performances of (a) CO, (b) C₃H₆, and (c) NO oxidation over Co₃O₄-F, Pt/Co₃O₄-F, Pt/Al₂O₃, Pt/SiO₂, and Pt/SiO₂ and Co₃O₄-F catalysts. The reaction conditions were as follows: 4000 ppm CO, 1000 ppm C₃H₆, 500 ppm NO, 10% O₂ balanced with N₂ at WHSV = 240,000 mL g⁻¹ h⁻¹. (d) The hydrothermal durability of Pt/Co₃O₄-F catalysts at 260 °C. The reaction conditions were as follows: 4000 ppm CO, 1000 ppm C₃H₆, 500 ppm NO, 10% O₂, and 5% H₂O balanced with N₂ at WHSV = 240,000 mL g⁻¹ h⁻¹.

To better understand the influence of CO, C₃H₆, and NO in simulated reactions, light-off tests were conducted under different atmospheres with single reactant or a mixture of CO and C₃H₆. As shown in Figure 2a, the Pt/Co₃O₄-F and Co₃O₄-F catalysts, which reached 90% conversion (T₉₀) at approximately 100 °C, performed much better single CO oxidation activities than the conventional Pt/Al₂O₃ catalysts. Even though the catalytic activity of single C₃H₆ oxidation on Pt/Al₂O₃ catalysts outperformed Pt/Co₃O₄-F and Co₃O₄-F (Figure 2b), the presence of CO extremely suppressed the C₃H₆ oxidation activity

over Pt/Al₂O₃ catalysts, which was demonstrated in Figure 2d. On the contrary, there was no apparent interference between C₃H₆ and CO over Pt/Co₃O₄-F and Co₃O₄-F catalysts (Figure 2c,d). Notably, NO was a severe inhibitor of catalytic oxidation reactions [13]. Consistent with the previous literature, NO intensively prohibited the CO oxidation activities among Pt/Co₃O₄-F, Co₃O₄-F, and Pt/Al₂O₃ catalysts. However, Pt/Co₃O₄-F and Co₃O₄-F exhibited better resistance on NO toward C₃H₆ oxidation. In contrast with Pt/Co₃O₄-F catalysts, NO acutely suppressed the activity of C₃H₆ oxidation over Pt/Al₂O₃ catalysts. Therefore, Pt/Co₃O₄-F and Co₃O₄-F catalysts obtained better catalytic oxidation activities and possessed superior resistance toward NO compared to the conventional Pt/Al₂O₃ catalysts.

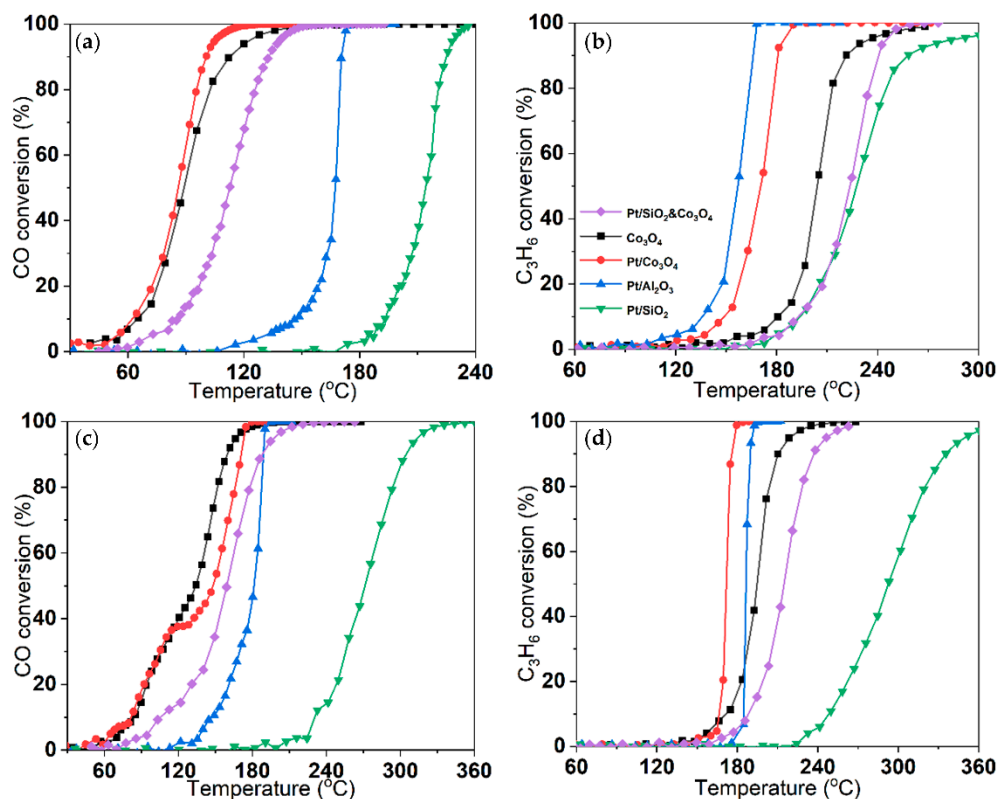


Figure 2. The light-off profiles of (a,c) CO oxidation and (b,d) C₃H₆ oxidation over Co₃O₄-F and Pt/Co₃O₄-F, Pt/Al₂O₃, Pt/SiO₂, and Pt/SiO₂ and Co₃O₄-F catalysts. The reaction conditions were as follows: (a) 4000 ppm CO, 10% O₂ balanced with N₂; (b) 1000 ppm C₃H₆, 10% O₂ balanced with N₂; and (c,d) 4000 ppm CO, 1000 ppm C₃H₆, 10% O₂ balanced with N₂. All the reactions were kept at WHSV = 240,000 mL g⁻¹ h⁻¹.

The addition of Pt also boosted the catalytic oxidation activities of NO and C₃H₆ in the low-temperature regime by taking advantage of SMSI between Pt and reducible Co₃O₄. Compared to Pt supported on the inert SiO₂, Pt/Co₃O₄-F exhibited dramatically better catalytic oxidation performances among CO, C₃H₆, and NO oxidations, which illustrated that the synergistic interactions between Pt and Co₃O₄ facilitated the oxidation process. According to the previous studies, SMSI generally occurred at the interface between noble metal and supporting reducible metal oxide [24]. Therefore, the physical mixing of Pt/SiO₂ and Co₃O₄-F catalysts (Pt/SiO₂ and Co₃O₄-F) were prepared and tested in different reactions. In comparison to Pt/Co₃O₄-F catalysts, Pt/SiO₂ and Co₃O₄-F catalysts displayed much lower catalytic activities toward CO, C₃H₆, and NO oxidations, which implied that SMSI only took place once Pt was in close proximity to the supporting Co₃O₄-F. Moreover, the Pt/SiO₂ and Co₃O₄-F catalysts demonstrated better activities than the Pt/SiO₂ catalysts, which could be due to the extraordinary oxidation ability of Co₃O₄-F.

2.2. Morphological and Textural Properties

The morphologies of $\text{Co}_3\text{O}_4\text{-F}$ catalysts were visualized via SEM techniques. As shown in Figure 3, the $\text{Co}_3\text{O}_4\text{-F}$ catalysts exhibited blooming flower structures with several petal-like nanosheets bundled together. The Pt/ $\text{Co}_3\text{O}_4\text{-F}$ catalysts demonstrated a nanoflower-like structure identical to $\text{Co}_3\text{O}_4\text{-F}$.

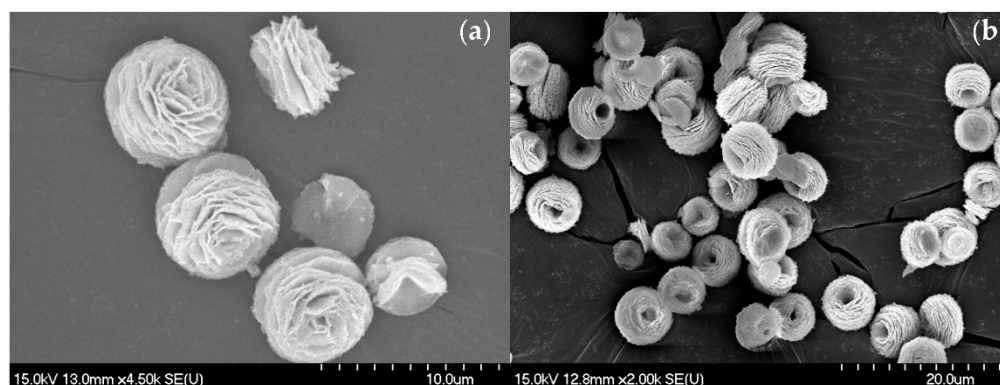


Figure 3. SEM images of $\text{Co}_3\text{O}_4\text{-F}$ with different scanning scales (a) 10 μm and (b) 20 μm .

Moreover, N_2 physisorption experiments were performed to investigate the textural properties of $\text{Co}_3\text{O}_4\text{-F}$ and Pt/ $\text{Co}_3\text{O}_4\text{-F}$ catalysts. As displayed in Figure 4, both $\text{Co}_3\text{O}_4\text{-F}$ and Pt/ $\text{Co}_3\text{O}_4\text{-F}$ catalysts demonstrated type IV isotherms with the H3 hysteresis loops, suggesting the formation of mesoporous structure on $\text{Co}_3\text{O}_4\text{-F}$ and Pt/ $\text{Co}_3\text{O}_4\text{-F}$ catalysts [25]. According to Table S2, $\text{Co}_3\text{O}_4\text{-F}$ and Pt/ $\text{Co}_3\text{O}_4\text{-F}$ catalysts exhibited BET surface areas of 30.4 and 30.2 $\text{m}^2 \text{g}^{-1}$, respectively. In addition, the pore volumes of $\text{Co}_3\text{O}_4\text{-F}$ and Pt/ $\text{Co}_3\text{O}_4\text{-F}$ were 0.089 and 0.090 $\text{cm}^3 \text{g}^{-1}$, respectively, indicating that the deposition of Pt did not influence the surface properties of $\text{Co}_3\text{O}_4\text{-F}$.

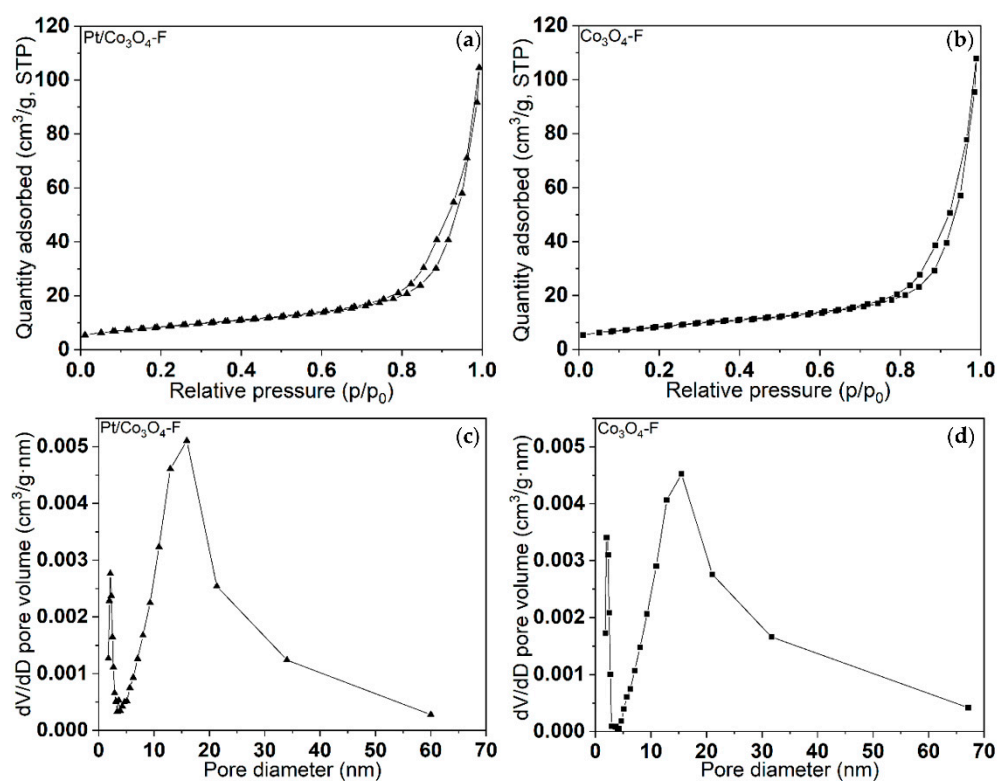


Figure 4. The N_2 adsorption–desorption isotherms and pore size distribution for (a,c) Pt/ $\text{Co}_3\text{O}_4\text{-F}$ and (b,d) $\text{Co}_3\text{O}_4\text{-F}$.

Furthermore, the XRD profiles of $\text{Co}_3\text{O}_4\text{-F}$ and $\text{Pt}/\text{Co}_3\text{O}_4\text{-F}$ catalysts are demonstrated in Figure 5. $\text{Pt}/\text{Co}_3\text{O}_4\text{-F}$ exhibited identical patterns in $\text{Co}_3\text{O}_4\text{-F}$ without any Pt diffraction peaks, suggesting that Pt particles are highly dispersed on the surface of $\text{Co}_3\text{O}_4\text{-F}$. In addition, the XRD profiles of $\text{Co}_3\text{O}_4\text{-F}$ and $\text{Pt}/\text{Co}_3\text{O}_4\text{-F}$ catalysts perfectly matched the standard reference patterns of spinel-structured Co_3O_4 (PDF#43-1003) with the space group $\text{Fd-}3\text{m}$ (227). The intensive XRD diffraction peaks, which appeared at 19.0° , 31.3° , 36.8° , 38.5° , 44.8° , 55.6° , 59.4° , 65.2° , and 77.3° , can be ascribed to crystal planes of (111), (220), (311), (222), (400), (422), (511), (440), and (533), respectively.

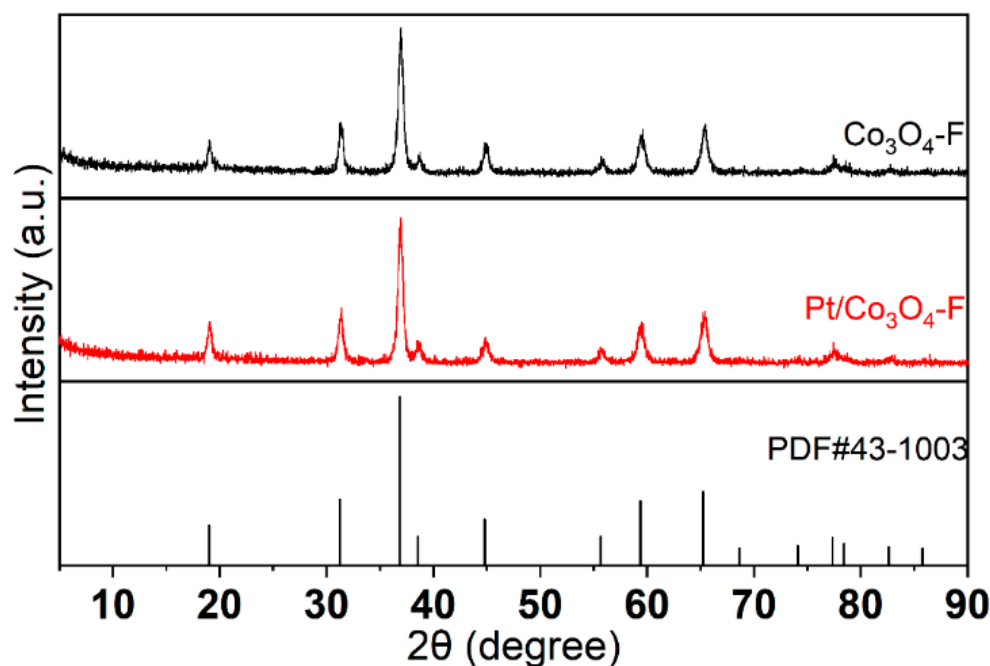


Figure 5. The XRD profiles of the $\text{Co}_3\text{O}_4\text{-F}$ and $\text{Pt}/\text{Co}_3\text{O}_4\text{-F}$ catalysts.

2.3. Surface Chemical Properties

XPS measurements were carried out to probe the surface valence states of different elements over the $\text{Co}_3\text{O}_4\text{-F}$ and $\text{Pt}/\text{Co}_3\text{O}_4\text{-F}$ catalysts. Figure 6a demonstrated the XPS spectra of $\text{Co } 2p_{3/2}$ for $\text{Co}_3\text{O}_4\text{-F}$ and $\text{Pt}/\text{Co}_3\text{O}_4\text{-F}$ catalysts, which were fitted into three intensive peaks and two broad shake-up satellite peaks. For $\text{Co}_3\text{O}_4\text{-F}$ catalysts, two shake-up satellite peaks at 789.9 and 785.7 eV could be due to Co^{2+} and Co^{3+} , respectively. Meanwhile, three characteristic peaks at approximately 781.9, 780.6, and 779.4 eV corresponded to Co^{2+} , Co^{3+} , and the combination of Co^{2+} and Co^{3+} , respectively [26]. As shown in Table 1, the addition of Pt atoms did not significantly affect the Co XPS pattern over $\text{Co}_3\text{O}_4\text{-F}$. Moreover, the XPS core-level spectra of O 1s for both catalysts (Figure 6b) were composed of a broad peak at 531.2 eV and a sharp peak at 529.9 eV, ascribed to chemisorbed or surface oxygen and lattice oxygen, respectively [27]. According to the relative area in Table 1, the deposition of Pt particles dramatically elevated the molar ratio of chemisorbed or surface oxygen from 38.6% to 50.1% over $\text{Pt}/\text{Co}_3\text{O}_4\text{-F}$, compared to $\text{Co}_3\text{O}_4\text{-F}$, which indicated the generation of more active surface oxygen species over $\text{Pt}/\text{Co}_3\text{O}_4\text{-F}$ catalysts. These active surface oxygen species might play a critical role in promoting the oxidation occurring over the surface of $\text{Pt}/\text{Co}_3\text{O}_4\text{-F}$ by being directly involved in the reaction [28]. Since the XPS core-level spectra of Co 2p did not show any significant difference between $\text{Co}_3\text{O}_4\text{-F}$ and $\text{Pt}/\text{Co}_3\text{O}_4\text{-F}$, the SMSI between Pt and supporting $\text{Co}_3\text{O}_4\text{-F}$ mainly elevated the amount of active surface oxygen over $\text{Pt}/\text{Co}_3\text{O}_4\text{-F}$.

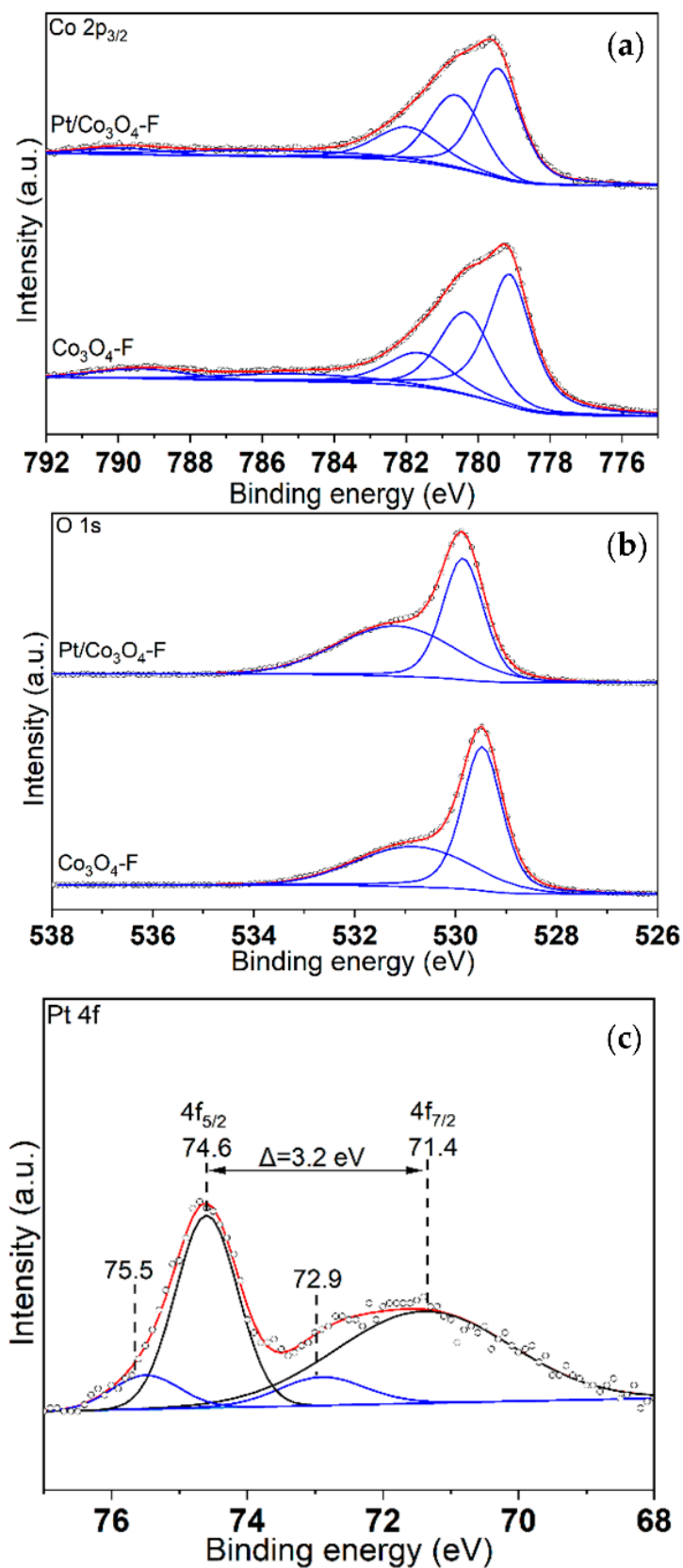


Figure 6. The deconvoluted peaks profiles of the (a) Co 2p_{3/2}, (b) O 1s, and (c) Pt 4f X-ray photoelectron spectra for Pt/Co₃O₄-F and Co₃O₄-F. Black dots: original data of XPS profiles; Blue lines: deconvoluted peaks of the XPS curves; Red line: fitting curves.

Table 1. The binding energy, FWHM, and relative area derived from the deconvoluted peaks of the Co 2p_{3/2} and O 1s spectra of the Pt/Co₃O₄-F and Co₃O₄-F catalysts.

Samples		Binding Energy (eV)	FWHM (eV)	Relative Area (%)	Assignment
Co 2p _{3/2}	Pt/Co ₃ O ₄ -F	779.4	1.47	42.1	Co ²⁺ and Co ³⁺
		780.6	1.72	27.2	Co ³⁺
		781.9	2.16	18.1	Co ²⁺
		785.7	6.97	8.9	Shake-up satellite
		789.9	2.73	3.7	Shake-up satellite
Co 2p _{3/2}	Co ₃ O ₄ -F	779.1	1.47	44.4	Co ²⁺ and Co ³⁺
		780.3	1.73	28.7	Co ³⁺
		781.6	2.14	15.5	Co ²⁺
		784.9	4.98	6.5	Shake-up satellite
		789.3	3.01	4.9	Shake-up satellite
O 1s	Pt/Co ₃ O ₄ -F	529.9	0.97	49.9	Lattice oxygen in spinel
		531.2	2.72	50.1	Chemisorbed and surface oxygen
O 1s	Co ₃ O ₄ -F	529.5	0.94	61.4	Lattice oxygen in spinel
		530.9	2.6	38.6	Chemisorbed and surface oxygen

As displayed in Figure 6c, Pt 4f core-level spectra demonstrated two intensive peaks at approximately 71.4 and 74.6 eV, which could be due to the binding energies of Pt 4f_{7/2} and Pt 4f_{5/2} for metallic Pt species [29]. Meanwhile, the spin-orbit components of Pt 4f core-level spectra could separate well with $\Delta_{\text{metal}} = 3.2$ eV [30]. These results proved that the metallic Pt species dominated the surface of the Pt/Co₃O₄-F catalysts.

2.4. Reducibility

H₂-TPR experiments were performed to investigate the reducibility of Co₃O₄-F and Pt/Co₃O₄-F catalysts. As shown in Figure 7, two well-resolved reduction peaks centered at approximately 340 and 422 °C were detected on Co₃O₄-F catalysts. The relatively weak peak I at 340 °C was the reduction of Co₃O₄ to CoO (Co₃O₄ + H₂ → 3CoO + H₂O). Meanwhile, the second broad peak at a higher temperature corresponded to the reduction process from CoO to metallic cobalt (CoO + H₂ → Co + H₂O) [31,32]. According to the detailed quantitative results from Table 2, the relative peak area ratio of peak I and peak II was equal to 3.29 for Co₃O₄-F catalysts, which was slightly larger than the theoretical ratio of 3.0, probably revealing an incomplete reduction of Co³⁺ to Co²⁺ during the first reduction peak. Compared to the Co₃O₄-F catalysts, the reduction processes over Pt/Co₃O₄-F shifted to much lower temperatures, with the first peak moving to 136 °C and the second peak to 326 °C. The left-shift of the reduction temperature was a typical signal for better reducibility. In addition, the relative area ratio between peak I and peak II decreased to 1.90, which was lower than the theoretical value of Co₃O₄-F and could be due to the following reasons. In regard to XPS results, SMSI between Pt and Co₃O₄-F generated active surface oxygen species over Pt/Co₃O₄-F, which coupled with H₂ at a relatively low-temperature range. Moreover, the synergistic interaction between Pt and Co₃O₄-F caused the complete reduction of Co₃O₄ to CoO, which increased the H₂ consumption of peak I. Meanwhile, the partial reduction of CoO to metallic Co might occur at the overlap area between peak I and peak II, at approximately 200 °C. Furthermore, the H₂ spillover might take place at the Pt/Co₃O₄-F interface, under a low-temperature regime as well. In summary, the significant shift of the reduction temperature indicated that the SMSI effect dramatically improved the reducibility over the surface of the Pt/Co₃O₄-F catalysts.

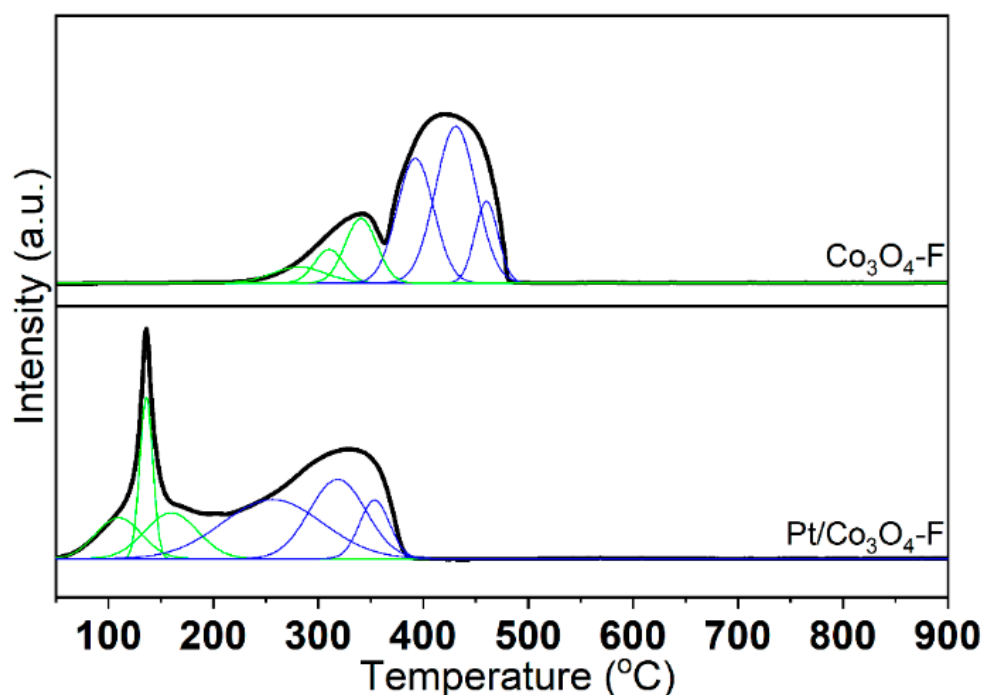


Figure 7. The H₂-TPR profiles of Co₃O₄-F and Pt/Co₃O₄-F. Black lines: original curves; Green and blue lines: deconvoluted peaks for the first and second reduction peak, respectively.

Table 2. The quantitative results of H₂-TPR of the Co₃O₄-F and Pt/Co₃O₄-F catalysts.

Catalysts	Deconvoluted Peaks			Peak Area Ratio of II/I
	Peak No.	Center (°C)	Area	
Co ₃ O ₄ -F	I	281.9	1.15	3.29
		310.3	1.31	
		340.7	2.73	
	II	392.5	6.10	
		431.0	8.48	
		460.2	2.51	
Pt/Co ₃ O ₄ -F	I	110.0	2.32	1.90
		136.2	2.60	
		160.1	3.01	
	II	256.4	7.33	
		318.5	5.54	
		353.7	2.17	

The thermogravimetric analysis was conducted under a nitrogen gas atmosphere to investigate the thermal properties of the Co₃O₄-F and Pt/Co₃O₄-F catalysts. As demonstrated in Figure 8, the weight losses below 700 °C were 0.79% and 1.17% for Co₃O₄-F and Pt/Co₃O₄-F, respectively, which illustrated that the addition of Pt atoms might promote the catalytic oxidation by advancing the desorption of nonstoichiometric oxygen species and surface-adsorbed hydroxyl radicals [33,34]. The weight loss above 700 °C could be due to the loss of lattice oxygen from Co₃O₄. For pure Co₃O₄-F catalysts, the weight loss caused by the release of lattice oxygen was approximately 6.2%, which was consistent with the stoichiometric decomposition of Co₃O₄ (Co₃O₄ → 3CoO + 1/2O₂). On the contrary, the weight loss for Pt/Co₃O₄-F (5.8 wt.%) was lower than the theoretical value, indicating that the Pt species were relatively stable in the high-temperature regime.

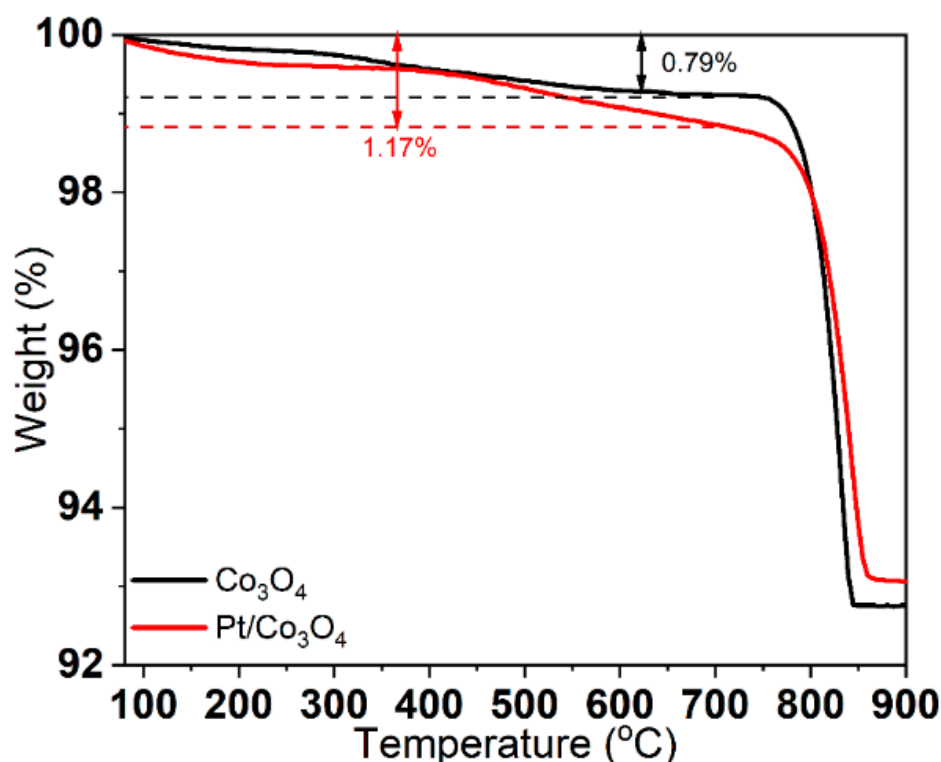


Figure 8. The thermo-gravimetric analysis profiles of the Co_3O_4 -F and $\text{Pt}/\text{Co}_3\text{O}_4$ -F catalysts under an N_2 atmosphere.

2.5. In Situ DRIFTS

To further probe the reaction mechanism over Co_3O_4 -F and $\text{Pt}/\text{Co}_3\text{O}_4$ -F catalysts, in situ DRIFTS experiments were carried out under different reactant atmospheres to analyze the surface-adsorbed molecules during the catalytic oxidation processes. As shown in Figure 9, abundant carbonated species located in the range from 1650 to 1200 cm^{-1} were observed during CO and O_2 co-adsorption at different temperatures over the surface of Co_3O_4 -F and $\text{Pt}/\text{Co}_3\text{O}_4$ -F. For both Co_3O_4 -F and $\text{Pt}/\text{Co}_3\text{O}_4$ -F catalysts, two intensive peaks at approximately 2114 and 2178 cm^{-1} could be due to the gaseous CO molecules and CO weakly adsorbed on defect sites on Co_3O_4 , respectively. Moreover, the weak peak around 2340 cm^{-1} was ascribed to the asymmetric stretching of generated CO_2 molecules [35]. As demonstrated in Figure 9a, plentiful bidentate carbonates (1618 , 1292 , and 1251 cm^{-1}) and free carbonate ions (1436 cm^{-1}) were detected over the surface of Co_3O_4 -F at $30\text{ }^\circ\text{C}$ [36]. The carbonate species were assigned as the indispensable intermediates to generate the final product of CO_2 since the signal of gaseous CO_2 was not detected at $30\text{ }^\circ\text{C}$. Meanwhile, the carbonate species were rapidly consumed, accompanied by the increased intensity of the CO_2 peak with the rising temperature. This phenomenon confirmed that the carbonate intermediates formed as the essential intermediates, which could be further oxidized to generate CO_2 . Over the surface of the $\text{Pt}/\text{Co}_3\text{O}_4$ -F catalysts (Figure 9b), there was an extra peak at approximately 2093 cm^{-1} , indicating the CO adsorbed on Pt particles. The major carbonates formed over $\text{Pt}/\text{Co}_3\text{O}_4$ -F catalysts at $30\text{ }^\circ\text{C}$ were monodentate carbonates (1324 and 1520 cm^{-1}) and free carbonate ions (1441 and 1398 cm^{-1}), along with a relatively low amount of bidentate carbonates (1259 cm^{-1}) [37]. The monodentate carbonate mainly adsorbed on the Pt species because it was not observed over pure Co_3O_4 -F catalysts. With the increasing temperature, the monodentate and free carbonate ions quickly faded. Additionally, the band position of the bidentate carbonates shifted from 1259 to 1223 cm^{-1} , which implied the surface-active oxygen species involved in the oxidation reaction [13].

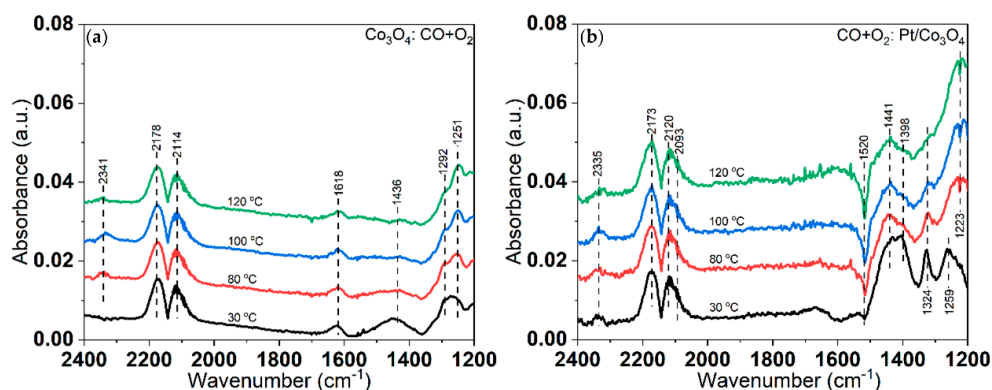


Figure 9. In situ DRIFTS spectra of CO and O₂ co-adsorption over (a) Co₃O₄-F and (b) Pt/Co₃O₄-F. The reaction conditions were as follows: 4000 ppm CO, 10% O₂, balanced with N₂, and the total flow rate was kept at 100 mL min⁻¹.

Figure 10 exhibited the CO and C₃H₆ co-oxidation over Co₃O₄-F and Pt/Co₃O₄-F catalysts at various temperatures. As shown in Figure 10a, the primary surface substances formed at 30 °C on Co₃O₄-F were gaseous CO (2113 cm⁻¹) and weakly surface bonded CO (2173 cm⁻¹), accompanied by bidentate carbonates (1637 cm⁻¹) and free carbonate ions (1445 cm⁻¹) formed through CO coupling with surface-active oxygen species. Once the temperature increased to 120 °C, the peak of gaseous CO₂ at 2330 cm⁻¹ appeared with the rapid consumption of carbonate species. Simultaneously, the appearance of intensive peaks located at 1540 and 1436 cm⁻¹ could be due to the formation of formate species, which were quickly depleted with the increasing temperature as the core intermediates during C₃H₆ oxidation [38,39]. Other than surface-adsorbed and gaseous CO molecules, monodentate carbonates (1326 cm⁻¹), carbonate free ions (1419 cm⁻¹), and bidentate carbonates (1609 cm⁻¹) were observed on the surface of Pt/Co₃O₄-F catalysts at 30 °C presented in Figure 10b. Meanwhile, the intensive peak at 1445 cm⁻¹ could be due to the CH₂ scissoring from C₃H₆ molecules adsorbed on Pt atoms [40]. Regarding CO oxidation, carbonate species quickly faded by reacting with the active oxygen to generate CO₂ (2331 cm⁻¹). Meanwhile, the formate species at 1542 cm⁻¹ were initially generated at 120 °C and then decomposed with the increasing temperature (HCO₂ → CO + OH). On the contrary, acetate species (1364 and 1433 cm⁻¹) gradually accumulated with the rising temperature due to their robust thermal stability below 300 °C [38]. Since the signal of adsorbed C₃H₆ was too weak to be detected over the surface of the Co₃O₄-F catalysts, this further confirmed that the Pt promoted C₃H₆ oxidation by working as the active site for the C₃H₆ adsorption and activation, which was consistent with the results of the catalytic activities.

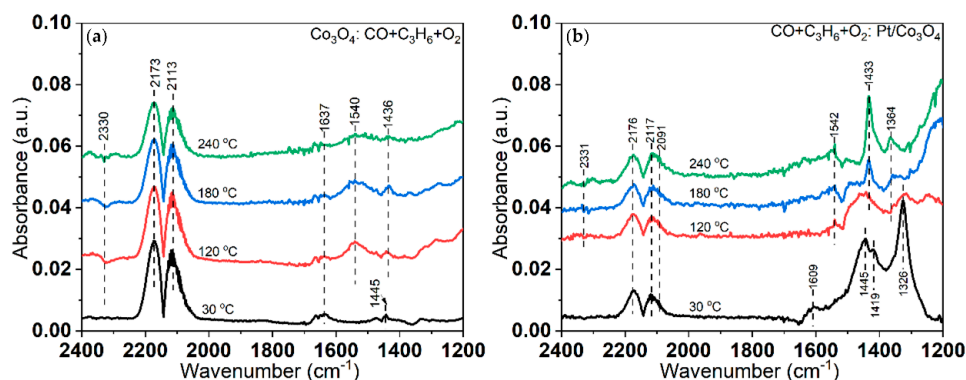


Figure 10. The in situ DRIFTS spectra of CO, C₃H₆, and O₂ co-adsorption over (a) Co₃O₄-F and (b) Pt/Co₃O₄-F. The reaction conditions were as follows: 4000 ppm CO, 1000 ppm C₃H₆, and 10% O₂, balanced with N₂, and the total flow rate was kept at 100 mL min⁻¹.

3. Materials and Methods

3.1. Preparation of Catalysts

The Co₃O₄ hierarchical nanoflower was synthesized by the hydrothermal method according to previous literature [20]. Typically, 0.8100 g of 2-methylimidazole (2-MIM) from Shanghai Aladdin Biochemical Technology Co., Ltd. (Shanghai, China) was dispersed in 25 mL of deionized water. Meanwhile, 0.2989 g of cobalt acetate tetrahydrate (Co(CH₃COO)₂·4H₂O) from Sinopharm Chemical Reagent Co., Ltd. (Beijing, China) was dissolved in 25 mL of deionized water. The solutions were vigorously stirred for 10 min. Then, Co(CH₃COO)₂·4H₂O solution was poured into 2-MIM solution and stirred for 5 min. Later, the mixed solution was aged at 125 °C for 1 h in a 100 mL Teflon-lined autoclave. After cooling to room temperature, the product was centrifuged and washed with deionized water at least four times. Finally, the product was dried at 70 °C overnight and calcined at 400 °C for 2 h ramped with 1 °C min⁻¹ to obtain Co₃O₄-F catalysts.

0.8 wt.% Pt/Co₃O₄-F catalysts were prepared by the incipient wetness impregnation method with Pt(NH₃)₄(NO₃)₂ (Sigma-Aldrich, Darmstadt, Germany) as the Pt precursor. Typically, 0.0205 mmol Pt(NH₃)₄(NO₃)₂ was dissolved in 30 mL deionized water, and then 0.5 g as-prepared Co₃O₄-F catalysts were dispersed into the solution. The mixture was intensively stirred for 10 h, and then the deionized water was evaporated at 70 °C. Subsequently, the mixture was dried at 100 °C overnight and then calcined at 400 °C for 6 h with a ramping rate of 1 °C min⁻¹ to fabricate Pt/Co₃O₄-F catalysts. Meanwhile, inductively coupled plasma-optical emission spectrometry (ICP-OES) experiments were carried out on Avio 500 (PerkinElmer Inc., Waltham, MA, USA) to investigate the elemental concentrations of platinum. As determined by the ICP-OES experiments, the platinum content of the Pt/Co₃O₄-F catalysts was 0.72 wt.%. In comparison, 2 wt.% Pt/Al₂O₃ and 2 wt.% Pt/SiO₂ catalysts were also prepared in agreement with our recent work [13,41].

3.2. Catalytic Oxidation Activity Tests

Reactant gases including 5% CO/N₂ (99.999%), 1% C₃H₆/N₂ (99.999%), 1% NO/N₂ (99.999%), high-purified O₂ (99.999%), and high-purified N₂ (99.999%) were purchased from Shanghai Weichuang Standard Gas Analytical Technology Co., Ltd (Shanghai, China). Moreover, mass flow controllers from Beijing Sevenstar Electronics Co., Ltd (Beijing, China) were applied to precisely manipulate the gas flow rate.

The catalytic activity tests were carried out in a fixed-bed quartz tube reactor sealed by quartz wool. The quartz sand (Innochem, Beijing, China), which was pretreated at 800 °C for 6 h in the static air, was used as the diluent. Before each test, all the samples were pretreated in pure N₂ (100 mL min⁻¹) at 300 °C for 1 h with a ramping rate of 2 °C min⁻¹ to remove any impurities and moisture. All the light-off experiments were performed with a ramp rate of 2 °C min⁻¹. For single CO or C₃H₆ light-off tests, reactant gases contained 4000 ppm CO or 1000 ppm C₃H₆, 10% O₂ balanced by N₂. For simulating the diesel emissions, a flowing mixture containing 4000 ppm CO, 1000 ppm C₃H₆, 500 ppm NO, and 10% O₂ in the presence or absence of 5% H₂O balanced with N₂ was purged into the reactor. Deionized water was injected into the reactor by the high-pressure syringe pump followed by the complete vaporization isothermal at 150 °C. The total flowrate of all reactions was fixed at 200 mL min⁻¹, corresponding to a weight hourly space velocity (WHSV) of 240,000 mL g⁻¹ h⁻¹. The concentration of reactant gases and products, including CO, C₃H₆, NO, and NO₂, was measured by an Antaris IGS Gas Analyzer (Thermo Fisher Scientific Inc., Waltham, MA, USA). The conversions of CO, C₃H₆, and NO were calculated by Equations (1)–(3).

$$X_{CO} = \frac{C_{CO,in} - C_{CO,out}}{C_{CO,in}} \times 100\%, \quad (1)$$

$$X_{C_3H_6} = \frac{C_{C_3H_6,in} - C_{C_3H_6,out}}{C_{C_3H_6,in}} \times 100\%, \quad (2)$$

$$X_{NO \rightarrow NO_2} = \frac{C_{NO_2,out} - C_{NO_2,in}}{C_{NO,in}} \times 100\%, \quad (3)$$

3.3. Characterizations

Powder X-ray diffraction (XRD) profiles of catalysts were measured on a Bruker-AXS D8 Advance X-ray diffractometer (Bruker Corporation, Billerica, MA, USA) using Cu K α radiation ($\lambda = 0.15406$ nm) at a tube voltage of 40 kV and a tube current of 30 mA, under an ambient atmosphere. The scan angle was recorded in the range from 5° to 90° with a step size of 0.02°, and it accumulated at a rate of 5° min⁻¹. The scanning electron microscopy (SEM) experiments were conducted via FEI Nano nova 450 (FEI, Marietta, GA, USA) to visualize the morphologies of the catalysts.

The N₂ adsorption–desorption isotherms were performed on a Micromeritics ASAP 2460 instrument (Micromeritics Instrument Corporation, Norcross, GA, USA) using N₂ as the carrier gas. Before the measurement, all the samples were degassed at 300 °C under a vacuum for 8 h. The Brunauer–Emmett–Teller (BET) equations were applied to calculate the surface area in the relative pressure (P/P_0) between 0.05 to 0.30. The Barrett–Joyner–Halenda (BJH) of the desorption curves were utilized to determine the pore size distributions.

X-ray Photoelectron Spectroscopy (XPS) tests were performed on a Kratos Axis Ultra DLD instrument (Shimadzu Corporation, Kyoto, Japan) using a monochromatic Al source with a working voltage and current of 14 kV and 8 mA, respectively. The carbon impurity with C1s at 284.8 eV was applied to calibrate the binding energies of all measured elements.

A temperature-programmed reduction by H₂ (H₂-TPR) was conducted on an Au-toChem II 2920 chemisorption analyzer (Micromeritics Instrument Corporation, Norcross, GA, USA). Typically, 60 mg catalysts were loaded into the U-shape quartz tube. Before each test, the samples were pretreated in a flow of 50 mL min⁻¹ Ar at 300 °C for 1 h to remove any impurities and moisture. After the system cooled down to 50 °C in the Ar atmosphere, 10% H₂/Ar (50 mL min⁻¹) was introduced to the system. Once the baseline was stable, the temperature was raised from 50 to 900 °C ramping with 10 °C min⁻¹. The consumption of H₂ was continuously monitored by the thermal conductivity detector.

A thermo-gravimetric analysis (TGA) was carried on a Differential Scanning Calorimetry-Mass instrument (Mettler Toledo, Greifensee, Switzerland). Before the experiments, all the catalysts were pretreated at 300 °C in a flow of N₂ (40 mL min⁻¹) to remove impurities and moistures. The tests were conducted under N₂ flow (40 mL min⁻¹) with the temperature rising from 50 to 900 °C at a ramping rate of 10 °C min⁻¹.

The in situ diffuse reflectance Fourier transform infrared spectroscopy (DRIFTs) studies were performed on a Nicolet 6700 spectrometer (Thermo Fisher Scientific Inc., Waltham, MA, USA) equipped with an MCT/A detector cooled by liquid nitrogen. To increase the absorbance intensity, Co₃O₄-based catalysts were diluted to a weight ratio of 10% by physically grinding with KBr powder in an agate mortar. Then, the fine ground catalyst powder was filled into the reaction chamber with BaF₂ windows embedded in the dome of the sample cell. Prior to the experiments, samples were pretreated in a pure N₂ flow (100 mL min⁻¹) at 300 °C for 1 h to remove the impurities and moistures. The background spectrum was recorded once the chamber cooled to the desired temperature and deducted from the sample spectrum at the same temperature during the reaction.

4. Conclusions

Flower-like Co₃O₄ catalysts were synthesized via the hydrothermal method. The results from SEM, XPS, and N₂ adsorption–desorption isotherms confirmed the formation of the uniformly structured nanoflower for both Co₃O₄ and Pt/Co₃O₄ catalysts. With the addition of Pt, Pt/Co₃O₄-F catalysts obtained excellent NO resistance and low-temperature catalytic oxidation performances toward multi-pollutants diesel emissions, which outperformed the commercial platinum DOCs. Moreover, the Pt/Co₃O₄-F catalysts exhibited the exceptional hydrothermal durability of CO, C₃H₆, and NO oxidation throughout an on-

stream test. Different characterization techniques were carried out to study SMSI between Pt and supporting $\text{Co}_3\text{O}_4\text{-F}$. The results of XPS spectra and $\text{H}_2\text{-TPR}$ profiles revealed that Pt boosted the chemisorbed capacity of oxygen on the surface of $\text{Co}_3\text{O}_4\text{-F}$ and enhanced the reducibility of the catalysts by taking advantage of the SMSI effect between Pt and supporting $\text{Co}_3\text{O}_4\text{-F}$, respectively. In addition, the TGA profiles proved that Pt promoted catalytic oxidation activities by increasing the desorption of surface-active oxygen and hydroxyl radicals at a relatively low-temperature regime. Furthermore, in situ DRIFTS spectra uncovered that CO and C_3H_6 firstly converted to carbonates, formate, and acetate species as the active intermediates and then further oxidized to generate CO_2 and H_2O as final products over Pt/ $\text{Co}_3\text{O}_4\text{-F}$. Meanwhile, compared to $\text{Co}_3\text{O}_4\text{-F}$ catalysts, metallic Pt atoms provided the active site for C_3H_6 adsorption and activation, which promoted the catalytic oxidation activity for C_3H_6 oxidation in the multi-pollutants exhaust.

Supplementary Materials: The following supporting information can be downloaded at: <https://www.mdpi.com/article/10.3390/catal12050527/s1>, Table S1: the comparison of catalytic activities of different catalysts toward CO, C_3H_6 and NO oxidation for multi-pollutant diesel emissions, Table S2: the N_2 adsorption–desorption isotherms of Pt/ $\text{Co}_3\text{O}_4\text{-F}$ and $\text{Co}_3\text{O}_4\text{-F}$. References [33,42–44] are cited in the supplementary materials.

Author Contributions: Conceptualization, L.M.; investigation, Z.L. and X.C.; data curation, Z.L. and X.C.; resources, J.C. and H.C.; writing—original draft, Z.L.; writing—review and editing, L.M. and N.Y.; supervision, L.M.; funding acquisition, L.M. All authors have read and agreed to the published version of the manuscript.

Funding: This work was financially supported by the National Natural Science Foundation of China (22176122), the Shanghai Pujiang Program (20PJ1407000), the special fund of the State Key Joint Laboratory of Environment Simulation and Pollution Control (21K07ESPCT), and the National Engineering Laboratory for Mobile Source Emission Control Technology (NELMS2018A12).

Data Availability Statement: The data presented in this study are available on request from the corresponding author.

Conflicts of Interest: The authors declare no conflict of interest.

References

1. Katare, S.R.; Patterson, J.E.; Laing, P.M. Diesel aftertreatment modeling: A systems approach to NO_x control. *Ind. Eng. Chem. Res.* **2007**, *46*, 2445–2454. [[CrossRef](#)]
2. Haaß, F.; Fuess, H. Structural characterization of automotive catalysts. *Adv. Eng. Mater.* **2005**, *7*, 899–913. [[CrossRef](#)]
3. Russell, A.; Epling, W.S. Diesel oxidation catalysts. *Catal. Rev.* **2011**, *53*, 337–423. [[CrossRef](#)]
4. Walker, A. Future challenges and incoming solutions in emission control for heavy duty diesel vehicles. *Top. Catal.* **2016**, *59*, 695–707. [[CrossRef](#)]
5. Pârvolescu, V.I.; Grange, P.; Delmon, B. Catalytic removal of NO. *Catal. Today* **1998**, *46*, 233–316. [[CrossRef](#)]
6. Li, Z.; Dai, S.; Ma, L.; Qu, Z.; Yan, N.; Li, J. Synergistic interaction and mechanistic evaluation of NO oxidation catalysis on Pt/ Fe_2O_3 cubes. *Chem. Eng. J.* **2021**, *413*, 127447. [[CrossRef](#)]
7. Chen, H.-Y.; Mulla, S.; Weigert, E.; Camm, K.; Ballinger, T.; Cox, J.; Blakeman, P. Cold start concept (CSCTM): A novel catalyst for cold start emission control. *SAE Int. J. Fuels Lubr.* **2013**, *6*, 372–381. [[CrossRef](#)]
8. Zammit, M.; DiMaggio, C.L.; Kim, C.H.; Lambert, C.; Muntean, G.G.; Peden, C.H.; Parks, J.E.; Howden, K. Future Automotive Aftertreatment Solutions: The 150 °C Challenge Workshop Report. Available online: https://cleers.org/wp-content/uploads/2012_The_150C_Challenge_Workshop_Report.pdf (accessed on 18 April 2022).
9. Liotta, L.F.; Wu, H.; Pantaleo, G.; Venezia, A.M. Co_3O_4 nanocrystals and $\text{Co}_3\text{O}_4\text{-MO}_x$ binary oxides for CO, CH_4 and VOC oxidation at low temperatures: A review. *Catal. Sci. Technol.* **2013**, *3*, 3085–3102. [[CrossRef](#)]
10. Xie, X.; Li, Y.; Liu, Z.-Q.; Haruta, M.; Shen, W. Low-temperature oxidation of CO catalysed by Co_3O_4 nanorods. *Nature* **2009**, *458*, 746–749. [[CrossRef](#)]
11. Ma, L.; Zhang, W.; Wang, Y.-G.; Chen, X.; Yu, W.; Sun, K.; Sun, H.; Li, J.; Schwank, J.W. Catalytic performance and reaction mechanism of NO oxidation over Co_3O_4 catalysts. *Appl. Catal. B Environ.* **2020**, *267*, 118371. [[CrossRef](#)]
12. Ma, L.; Geng, Y.; Chen, X.; Yan, N.; Li, J.; Schwank, J.W. Reaction mechanism of propane oxidation over Co_3O_4 nanorods as rivals of platinum catalysts. *Chem. Eng. J.* **2020**, *402*, 125911. [[CrossRef](#)]
13. Ma, L.; Seo, C.Y.; Chen, X.; Sun, K.; Schwank, J.W. Indium-doped Co_3O_4 nanorods for catalytic oxidation of CO and C_3H_6 towards diesel exhaust. *Appl. Catal. B Environ.* **2018**, *222*, 44–58. [[CrossRef](#)]

14. Tauster, S.J.; Fung, S.C.; Baker, R.T.K.; Horsley, J.A. Strong interactions in supported-metal catalysts. *Science* **1981**, *211*, 1121–1125. [[CrossRef](#)] [[PubMed](#)]
15. Gatla, S.; Aubert, D.; Agostini, G.; Mathon, O.; Pascarelli, S.; Lunkenbein, T.; Willinger, M.G.; Kaper, H. Room-temperature CO oxidation catalyst: Low-temperature metal–support interaction between platinum nanoparticles and nanosized ceria. *ACS Catal.* **2016**, *6*, 6151–6155. [[CrossRef](#)]
16. DeRita, L.; Dai, S.; Lopez-Zepeda, K.; Pham, N.; Graham, G.W.; Pan, X.; Christopher, P. Catalyst architecture for stable single atom dispersion enables site-specific spectroscopic and reactivity measurements of CO adsorbed to Pt atoms, oxidized Pt clusters, and metallic Pt clusters on TiO₂. *J. Am. Chem. Soc.* **2017**, *139*, 14150–14165. [[CrossRef](#)]
17. Lewandowski, M.; Sun, Y.N.; Qin, Z.H.; Shaikhutdinov, S.; Freund, H.J. Promotional effect of metal encapsulation on reactivity of iron oxide supported Pt catalysts. *Appl. Catal. A Gen.* **2011**, *391*, 407–410. [[CrossRef](#)]
18. Zhao, J.; Tang, Z.; Dong, F.; Zhang, J. Controlled porous hollow Co₃O₄ polyhedral nanocages derived from metal-organic frameworks (MOFs) for toluene catalytic oxidation. *Mol. Catal.* **2019**, *463*, 77–86. [[CrossRef](#)]
19. Zhao, S.; Li, T.; Lin, J.; Wu, P.; Li, Y.; Li, A.; Chen, T.; Zhao, Y.; Chen, G.; Yang, L.; et al. Engineering Co³⁺-rich crystal planes on Co₃O₄ hexagonal nanosheets for CO and hydrocarbons oxidation with enhanced catalytic activity and water resistance. *Chem. Eng. J.* **2021**, *420*, 130448. [[CrossRef](#)]
20. Niu, H.; Wu, Z.; Hu, Z.-T.; Chen, J. Imidazolate-mediated synthesis of hierarchical flower-like Co₃O₄ for the oxidation of toluene. *Mol. Catal.* **2021**, *503*, 111434. [[CrossRef](#)]
21. Zhang, S.; Li, X.-S.; Chen, B.; Zhu, X.; Shi, C.; Zhu, A.-M. CO oxidation activity at room temperature over Au/CeO₂ catalysts: Disclosure of induction period and humidity effect. *ACS Catal.* **2014**, *4*, 3481–3489. [[CrossRef](#)]
22. Gélín, P.; Urfels, L.; Primet, M.; Tena, E. Complete oxidation of methane at low temperature over Pt and Pd catalysts for the abatement of lean-burn natural gas fuelled vehicles emissions: Influence of water and sulphur containing compounds. *Catal. Today* **2003**, *83*, 45–57. [[CrossRef](#)]
23. Indarto, A. Heterogeneous reactions of HONO formation from NO₂ and HNO₃: A review. *Res. Chem. Intermed.* **2012**, *38*, 1029–1041. [[CrossRef](#)]
24. Willinger, M.G.; Zhang, W.; Bondarchuk, O.; Shaikhutdinov, S.; Freund, H.-J.; Schlögl, R. A case of strong metal–support interactions: Combining advanced microscopy and model systems to elucidate the atomic structure of interfaces. *Angew. Chem. Int. Ed.* **2014**, *53*, 5998–6001. [[CrossRef](#)]
25. Sing, K.S.W. Reporting physisorption data for gas/solid systems with special reference to the determination of surface area and porosity. *Pure Appl. Chem.* **1985**, *57*, 603–619. [[CrossRef](#)]
26. Cabrera-German, D.; Gomez-Sosa, G.; Herrera-Gomez, A. Accurate peak fitting and subsequent quantitative composition analysis of the spectrum of Co 2p obtained with Al K α radiation: I: Cobalt spinel. *Surf. Interface Anal.* **2016**, *48*, 252–256. [[CrossRef](#)]
27. Langell, M.A.; Kim, J.G.; Pugmire, D.L.; McCarroll, W. Nature of oxygen at rocksalt and spinel oxide surfaces. *J. Vac. Sci. Technol. A* **2001**, *19*, 1977–1982. [[CrossRef](#)]
28. Bai, B.; Arandiyani, H.; Li, J. Comparison of the performance for oxidation of formaldehyde on nano-Co₃O₄, 2D-Co₃O₄, and 3D-Co₃O₄ catalysts. *Appl. Catal. B Environ.* **2013**, *142–143*, 677–683. [[CrossRef](#)]
29. Zhou, Y.; Perket, J.M.; Zhou, J. Growth of Pt nanoparticles on reducible CeO₂(111) thin films: Effect of nanostructures and redox properties of ceria. *J. Phys. Chem. C* **2010**, *114*, 11853–11860. [[CrossRef](#)]
30. Hüfner, S.; Wertheim, G.K. Core-line asymmetries in the X-ray-photoemission spectra of metals. *Phys. Rev. B* **1975**, *11*, 678–683. [[CrossRef](#)]
31. Zhao, S.; Hu, F.; Li, J. Hierarchical core–shell Al₂O₃@Pd-CoAlO microspheres for low-temperature toluene combustion. *ACS Catal.* **2016**, *6*, 3433–3441. [[CrossRef](#)]
32. Pu, Z.; Liu, Y.; Zhou, H.; Huang, W.; Zheng, Y.; Li, X. Catalytic combustion of lean methane at low temperature over ZrO₂-modified Co₃O₄ catalysts. *Appl. Surf. Sci.* **2017**, *422*, 85–93. [[CrossRef](#)]
33. Li, P.; Chen, X.; Ma, L.; Bhat, A.; Li, Y.; Schwank, J.W. Effect of Ce and La dopants in Co₃O₄ nanorods on the catalytic activity of CO and C₃H₆ oxidation. *Catal. Sci. Technol.* **2019**, *9*, 1165–1177. [[CrossRef](#)]
34. Feng, J.; Zeng, H.C. Size-controlled growth of Co₃O₄ nanocubes. *Chem. Mater.* **2003**, *15*, 2829–2835. [[CrossRef](#)]
35. Lin, H.-K.; Wang, C.-B.; Chiu, H.-C.; Chien, S.-H. In situ FTIR study of cobalt oxides for the oxidation of carbon monoxide. *Catal. Lett.* **2003**, *86*, 63–68. [[CrossRef](#)]
36. Hertl, W. Infrared spectroscopic study of catalytic oxidation reactions over cobalt oxide under steady-state conditions. *J. Catal.* **1973**, *31*, 231–242. [[CrossRef](#)]
37. Hadjiivanov, K.I.; Vayssilov, G.N. Characterization of oxide surfaces and zeolites by carbon monoxide as an IR probe molecule. *Adv. Catal.* **2002**, *47*, 307–511.
38. Finocchio, E.; Busca, G.; Lorenzelli, V.; Escribano, V.S. FTIR studies on the selective oxidation and combustion of light hydrocarbons at metal oxide surfaces. Part 2.—Propane and propene oxidation on Co₃O₄. *J. Chem. Soc. Faraday Trans.* **1996**, *92*, 1587–1593. [[CrossRef](#)]
39. Busca, G.; Lamotte, J.; Lavalley, J.C.; Lorenzelli, V. FT-IR study of the adsorption and transformation of formaldehyde on oxide surfaces. *J. Am. Chem. Soc.* **1987**, *109*, 5197–5202. [[CrossRef](#)]
40. Zaera, F.; Chrysostomou, D. Propylene on Pt(111). *Surf. Sci.* **2000**, *457*, 71–88. [[CrossRef](#)]

41. Li, Z.; Geng, Y.; Ma, L.; Chen, X.; Li, J.; Chang, H.; Schwank, J.W. Catalytic oxidation of CO over Pt/Fe₃O₄ catalysts: Tuning O₂ activation and CO adsorption. *Front. Environ. Sci. Eng.* **2020**, *14*, 65. [[CrossRef](#)]
42. Ho, P.H.; Woo, J.-W.; Feizie Ilmasani, R.; Han, J.; Olsson, L. The role of Pd–Pt interactions in the oxidation and sulfur resistance of bimetallic Pd–Pt/γ-Al₂O₃ diesel oxidation catalysts. *Ind. Eng. Chem. Res.* **2021**, *60*, 6596–6612. [[CrossRef](#)]
43. Glover, L.; Douglas, R.; McCullough, G.; Keenan, M.; Revereault, P.; McAtee, C. Performance characterisation of a range of diesel oxidation catalysts: effect of Pt:Pd ratio on light off behaviour and nitrogen species formation. *SEA Int.* **2011**. [[CrossRef](#)]
44. Hazlett, M.J.; Moses-Debusk, M.; Parks II, J.E.; Allard, L.F.; Epling, W.S. Kinetic and mechanistic study of bimetallic Pt-Pd/Al₂O₃ catalysts for CO and C₃H₆ oxidation. *Appl. Catal. B Environ.* **2017**, *202*, 404–417. [[CrossRef](#)]